Automated Segmentation of the Prostate in 3D MR Images Using a Probabilistic Atlas and a Spatially Constrained Deformable Model — Source link ⬀

Sébastien Martin, Jocelyne Troccaz, Vincent Daanen

Institutions: Centre national de la recherche scientifique

Topics: Scale-space segmentation, Image segmentation, Active appearance model, Segmentation and Image registration

Related papers:

- Automatic segmentation of the prostate in 3D MR images by atlas matching using localized mutual information.

- Multifeature Landmark-Free Active Appearance Models: Application to Prostate MRI Segmentation

- Label Fusion in Atlas-Based Segmentation Using a Selective and Iterative Method for Performance Level Estimation (SIMPLE)

- Evaluation of prostate segmentation algorithms for MRI: the PROMISE12 challenge.

- Measures of the Amount of Ecologic Association Between Species

Automated Segmentation of the Prostate in 3D MR Images Using a Probabilistic Atlas and a Spatially Constrained Deformable Model

Sébastien Martin, Vincent Daanen, Jocelyne Troccaz

Automated Segmentation of the Prostate in 3D MR Images Using a Probabilistic Atlas and a Spatially Constrained Deformable Model

Sébastien Martin, Vincent Daanen, Jocelyne Troccaz

February 16, 2010

Abstract

Purpose: We present a fully automatic algorithm for the segmentation of the prostate in three-dimensional magnetic resonance (MR) images.

Method: Our approach requires the use of an anatomical atlas which is built by computing transformation fields mapping a set of manually segmented images to a common reference. These transformation fields are then applied to the manually segmented structures of the training set in order to get a probabilistic map on the atlas.

The segmentation is then realized through a two stage procedure. In the first stage, the processed image is registered to the probabilistic atlas. Subsequently, a *probabilistic segmentation* is obtained by mapping the probabilistic map of the atlas to the patient's anatomy. In the second stage, a deformable surface evolves towards the prostate boundaries by merging information coming from the *probabilistic segmentation*, an *image feature model* and a *statistical shape model*. During the evolution of the surface, the *probabilistic segmentation* allows the introduction of a *spatial constraint* that prevents the deformable surface from leaking in an unlikely configuration.

Results: The proposed method is evaluated on 36 exams, that were manually segmented by a single expert. A median Dice similarity coefficient of 0.86 and an average surface error of 2.41 mm are achieved.

Conclusion: By merging prior knowledge, the presented method achieves a robust and completely automatic segmentation of the prostate in MR images. Results show that the use of a *spatial constraint* is useful to increase the robustness of the deformable model comparatively to a deformable surface that is only driven by an image appearance model.

1   Introduction

1.1   Context

Segmentation of medical images is the preliminary step in many high-level tasks such as computer-assisted diagnosis, computer-assisted surgery or construction of bio-mechanical models. Segmentation of some modalities such as Magnetic Resonance Images, however, remains an open issue. Indeed, the complex nature of images (e.g. ill-defined boundary, low contrast, etc.) and shapes can make the image segmentation process inaccurate and non-robust. To overcome these limitations automatic segmenta-

tion algorithms make an intensive use of shape and appearance models.

Among the segmentation algorithms that incorporate a high level of prior knowledge, approaches based on the use of anatomical atlases have been extensively studied particularly for segmenting MR brain images [13]. *Atlas-based methods* solve the segmentation problem by registering a target image (to be segmented) to a labeled image (atlas). One of the benefits of using *atlas-based methods* is the introduction of a high level of prior knowledge on the spatial relationships between anatomical structures. Even when only one structure has to be segmented in the image, all the objects in the atlas image implicitly contribute to the segmentation process. Another interest in using *atlas-based methods* is to exploit their ability to extract a complete distribution of the probability that a voxel belongs to one or more organs (*probabilistic segmentation*). In this case, the so called *probabilistic atlas* is a powerful method of extracting a priori information on the location of anatomical structures which can then be used by another segmentation method [18].

Deformable surfaces is another type of segmentation method which has been often used for the delineation of tri-dimensional structures [24, 5]. A strong reason for using deformable surfaces is the introduction of prior knowledge about the shape of the target object [3, 29, 15]. Furthermore, these methods are well suited to building an image appearance model and constitute an appropriate framework for merging different sources of information [19].

In this paper, we propose a two stage method for segmenting prostate MR images. Before applying the segmentation method, we have computed a *probabilistic atlas* by mapping a population of manually segmented MR exams onto a single reference individual exam [18]. During the first stage of the method, the new patient to be segmented is registered to the probabilistic atlas using an intensity-based registration. The anatomical atlas embeds probabilistic spatial priors on the location of the prostate which are used to get a probabilistic segmentation of the patient image. Then, during the second stage, a deformable surface evolves towards the prostate boundaries. External forces which drive the deformable surface are extracted from the image data and the *probabilistic segmentation* obtained in the previous stage. This strategy prevents the model from leaking in an unlikely configuration by *spatially constraining* the evolution of the deformable surface. To further improve the robustness of the method, internal forces are used to incorporate prior knowledge on the prostate shape. Fig. 1 shows a schematic overview of the method.

While, in the past, several groups have combined the power of *anatomical atlases* and *deformable models* for the segmentation of anatomical structures, they limited the use of anatomical atlases to the initialization of deformable models [5, 19]. However, we think that *probabilistic segmentations* bring valuable information that can prevent the segmentation from deteriorating when the prostate capsule does not appears in the image or when "false boundaries" lie in the vicinity of the surface.

1.2   Issues

Our data base is composed of 36 MR exams of patients with a suspected prostate cancer. Mainly due to the presence of a large anatomical variability [28], the segmentation of these images is a challenging task. This anatomical variability includes both a variability of the prostate shape and a variability of its appearance in the images.

2

level 1 : Atlas matching

ATLAS

mean Image   Prob. Map

Registration

Patient Volume

level 2 : Deformable Surface Model

- Image Feature Model
- Spatial Constraint Model
- Statistical Shape Model

Prob. Segmentation

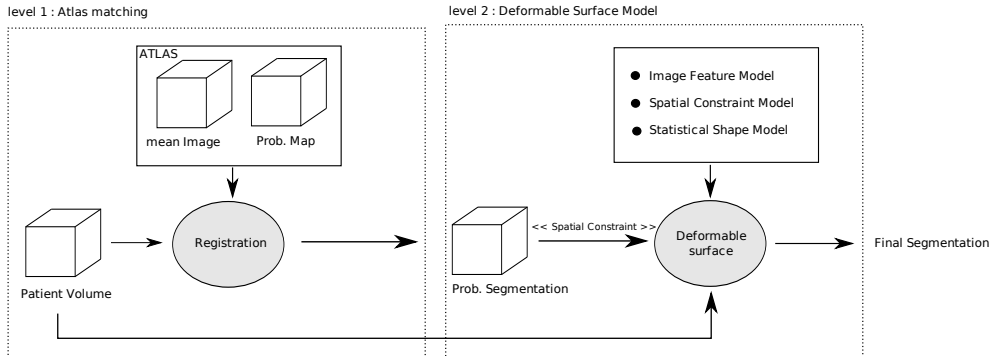<< Spatial Constraint >>

Deformable surface

Final Segmentation

Figure 1: **The segmentation method diagram**

Large prostate volume variations that can be observed with a minimum volume of 22 cc up to a maximum volume of 120 cc and the large differences in bladder and rectum filling (see Fig. 2), bring out the heterogeneity of the data set.

Moreover, the segmentation is made even more challenging by the presence of image artifacts caused by inhomogeneities in the magnetic field, and the use of MR scans with highly anisotropic voxels (0.5mm $\times$ 0.5mm $\times$ 3.3mm). Fig. 2 illustrates some of these issues.

1.3   Previous Work

Prostatic adenocarcimona is the second most common cancer in men. It is the second leading cause of cancer death among men in the US [9].

Previous work on prostate segmentation have focused mostly on transrectal ultrasound (TRUS) imaging and computed tomography (CT) imaging which are extensively used for cancer detection and treatment [24, 5].

However, in recent years, MR imaging has received increasing interest. Several studies show that the use of additional information from MR imaging can reduce inter-observer variability of prostate delineation in CT images or TRUS images and thus improve the treatment planning [20, 6]. Moreover, new MR modalities such as MR spectroscopy (MRS), dynamic contrast enhanced MRI (DCE-MRI) with gadolinium injection or lymphotrophic nanoparticle enhanced MRI (LN-MRI) have emerged as new, promising methods for the detection of prostate cancer. These methods could potentially improve the sensitivity and specificity of cancer detection [23, 7, 8]. In this context, the segmentation of the prostate in MR images is critical for a large number of problems such as volume estimation or multi-modal image fusion (MR/US, MR/CT) [20].

Few approaches have been proposed for the segmentation of the prostate in MRI; they fall into two categories. The first category of methods is based on the use of anatomical atlases. In [11] the segmentation is realized in two steps. First, a set of labeled individual images are registered onto the target patient image. Second, the deformed atlas label images are fused to yield a single segmentation of the patient im-

3

age. Although multi-atlas methods can be potentially interesting to improve the segmentation accuracy in the case of a large anatomical variability, we have first focused in this paper on the use of a single *probabilistic atlas*. This atlas, however, is only used to constrain the evolution of the deformable surface and not as a standalone method. In our previous work [12], we proposed an atlas based method for semi-automatic segmentation of the prostate in MR images. The segmentation was realized by registering an anatomical atlas onto a patient image using an intensity based registration that can handles user-provided geometric constraints. These geometric constraints were used to improve the registration accuracy and thus obtain more accurate segmentations. In a second step, the obtained surface was projected onto the shape space spanned by a statistical model to ensure that the final segmentation was statistically plausible. In the present work, the segmentation is mostly handled by a deformable surface. An anatomical atlas is used to provide a probabilistic segmentation that is used to constrain the evolution of the deformable model. Note that no deformable surface was used in our previous work.

The second category of methods is based on the use of a deformable surface. In [27] an automatic segmentation of the prostate is realized in two steps; in the first step, a clustering algorithm operating on MRS data is used to isolate the region of interest (ROI) of the prostate. In the second step, an Active Shape Model (ASM) is initialized within the ROI and used to obtain the final segmentation. Although this work proposed an interesting method for deformable model initialization, the clustering step operates on spectroscopic data and is thus not usable for standard MRI. In [1], a manually initialized ASM is used to achieve a semi-automatic segmentation of the prostate. The external forces which drive the deformable model toward the prostate boundaries are based on the image gradient. In our opinion, the image gradient is not suitable for capturing the prostate boundary that can appear in the image at some locations as a ridge or disappear in other locations. In [30] a semi-automatic segmentation method, based on hybrid 2D/3D ASM is used to deal with sparse 3D data. A 2D ASM that operates on each slice and 3D ASM are combined to obtain a "global optimal" segmentation. This method is well suited to deal with MR acquisitions with highly anisotropic voxels. However, in the future, MR acquisitions could be easily realized with non anisotropic voxels as in [11]. Consequently we focused on a purely 3D approach rather than a hybrid 2D/3D method.

The major advantage of the second category of methods is their ability to incorporate prior knowledge on the prostate's shape. However, the segmentation accuracy usually depends highly on the quality of the initialization as well as on the robustness of the detection of the prostate boundaries. In this paper, the deformable surface is initialized using the patient-to-atlas registration transform. This leads to an automatic segmentation, desirable since semi-automatic methods are time consuming. Moreover, to increase the robustness of the detection of prostate boundaries, we take advantage of the *probabilistic segmentation* by using a *Spatial Constraint Model* that ensures that the deformable surface stays in a likely configuration.

The paper is organized as follows. Sec. 2 is devoted to the description of first level of the method, called "Atlas Matching" (see Fig. 1). In this section, we first review the demon algorithm (2.1) and then describe the atlas construction

(2.2) and the matching of the new patient image to the anatomical atlas (2.3). Sec. 3 is dedicated to the description of the second level of the method, called "Deformable Surface Model" (see Fig. 1). In this section, we first present our deformable surface framework (3.2), and then describe the detection of the prostate boundaries (3.3) and the evolution of the deformable surface (3.4) which follows a coarse-to-fine approach. The last subsection (3.5) gives some details on the method used for establishing correspondence across shapes in order to build Statistical Models. Finally, Sec. 4 presents the results obtained and discusses results and possible improvements.

2 Level 1: Atlas Matching

2.1 Multi-Resolution Demons Registration

The demons algorithm [26] is a widely used image registration method. The algorithm approaches the problem of matching a template image onto a reference image as a diffusion process. The displacement field is computed on a regular grid with one displacement vector per voxel.

A set of forces (so-called demons) are computed at each node of the grid and act as effectors that drive the registration process. Most often, the design of *demons* is based on the minimization of the quadratic distance between the two images, but various similarity measures can be considered. The diffusion process can be envisioned at two different levels. First, a diffusion of the demons field can be realized. This step ensures the first level of regularization often called fluid-like regularization. A second diffusion can act on the displacement field. This step ensures the second level of regularization often called diffusion-like regularization. This diffusion can

be seen as a rough modeling of an elastic behavior. Let M be the moving image and F be the fixed image where $M, F : \Omega \rightarrow \mathbf{R}$. We refer to the demons field (force field) as $v : \Omega \rightarrow \mathbf{R}^3$ and the transformation as $s : \Omega \rightarrow \mathbf{R}^3$. Moreover, let $c : \Omega \rightarrow \mathbf{R}^3$ be an auxiliary vector field. The non rigid registration algorithm aims to determine the transformation $s(x)$ in order to get a reasonable alignment between the wrapped image $M \circ s(x)$ and the fixed image:

Demons algorithm

Iterate until convergence

- *Given s, compute the demons field v :*
  $v \leftarrow k(M \circ s - F)\nabla(M \circ s)$
  where k is a scalar that is tuned to get a maximum displacement of 0.5 voxel.

- *Process a fluid-like regularization using a Gaussian kernel K_{fluid} :*
  Let $u \leftarrow K_{fluid} \star v$.

- *Update the registration transform using a compositive scheme :*
  Let $c \leftarrow s \circ (x + u(x))$

- *Process a diffusion-like regularization using a Gaussian kernel K_{diff} :*
  let $s \leftarrow x + K_{diff} \star (c(x) - x)$.

The algorithm uses the Sum of the Squared Distance (SSD) as similarity criterion. The optimization is based on a gradient descent on the SSD using a "compositive scheme" [25]. An histogram matching is performed, between the two images, before each registration [17]. This process compensates for differences in intensity distribution that can occur between images and thus makes the SSD usable for inter-subject registration.

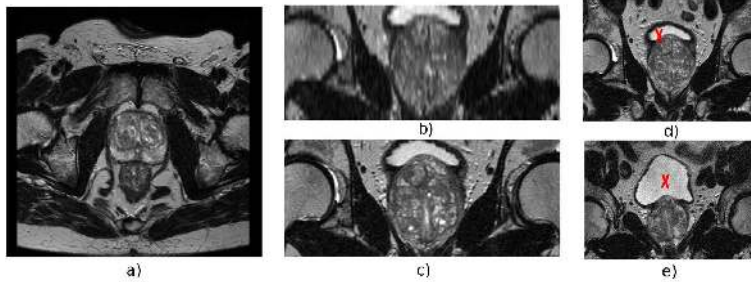A pyramidal approach is used to improve the speed of the algorithm and prevents the underly-

Figure 2: **Acquisition with strongly anisotropic voxels. (a)** transverse slice with a pixel size of 0.5 mm × 0.5 mm ; **(c)** coronal slice with a pixel size of 0.5 mm × 0.5 mm ; **(b)** same coronal slice as (c) reconstructed from a transverse volume with a voxel size of 0.5 mm × 0.5 mm × 3.5 mm. **Illustration of differences in bladder filling. (d)** and **(e)** : two different exams (coronal view), the bladder is marked with a red cross

ing energy minimization from falling into a local minimum. The registration process starts at the coarse scale and ends when the convergence level is reached. Then, the registration transform determined at the coarse level is used to initialize the registration transform at the next finer level. This process is repeated until the finest scale is reached. In practice we use 4 levels.

2.2 Atlas construction

Our probabilistic atlas is composed of a *mean image* $\bar{I}(x)$ associated with a *probability map* $\mathcal{P}(x)$. $\mathcal{P}(x)$ represents the likelihood of finding the prostate at a specified position for a subject that has been aligned to $\bar{I}(x)$ using a specific image registration algorithm.

The construction process is based on the alignment of a set of $\mathcal{N}$ manually segmented MR exams onto a common reference [18]. In a first step, each patient image is registered to a reference image using an affine intensity registration followed by a non-rigid demons-based registration.

An arbitrary choice of the reference image can introduce a bias in the construction process. To reduce this bias, the reference image is manually chosen amongst the population such that the prostate volume of the reference is closed to the mean prostate volume of the population. The mean image $\bar{I}$ is then computed by averaging all patient images aligned to the reference image.

In a second step, each patient image is registered to the mean image using the same registration algorithm as previously. The *probability map* is then obtained by averaging deformed patient label images

$$\mathcal{P}(x) = \frac{1}{\mathcal{N}} \sum_{i=1}^{\mathcal{N}} L_i \circ T_{i \rightarrow ATLAS}, \qquad (1)$$

where $T_{i \rightarrow ATLAS}$ is the registration transform that maps the patient image i to the mean image and $L_i(x)$ is the label image of the patient i. It is important to note that the transformation $T_{i \rightarrow ATLAS}$ results from an affine followed by a nonrigid registration. $L_i(x)$ has a value of 1.0 for all voxels labeled as belonging to the prostate
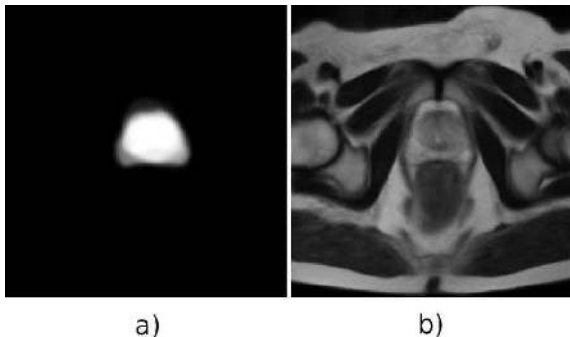
Figure 3: **Atlas obtained using our framework**. (a) Transverse slice of the probability map obtained using our method. (b) Transverse slice of the mean image obtained using our method.

and the value of 0.0 for all other voxels. An example of a resulting atlas is presented in Fig. 3.

2.3 Atlas Matching

The new patient to be segmented is first registered to the mean image $\bar{I}$ using the registration algorithm used to build the probability map (same parameters). After the registration, a probabilistic segmentation is obtained by mapping the atlas probability to the patient image using the inverse registration transform. At the end of this stage, a first segmentation can be obtained by considering a voxel inside the prostate if its probability of belonging to the prostate is greater than its probability of belonging to the background, i.e. if $\mathcal{P}(x) > 0.5$

3 Level 2: Deformable Model

3.1 Overview

After the matching of the new patient image to the anatomical atlas, a triangulation of the average shape of the prostate (i.e the atlas probability map thresholded to 0.5) is propagated to the patient anatomy by applying to it the registration transform. This *deformed mesh* is used for the initialization of the deformable model and then evolves towards the prostate boundaries by merging information coming from :

- An Image Feature Model

- A Spatial Constraint Model

- A Statistical Shape Model (SSM)

3.2 Deformable Surface Framework

This section is devoted to the description of the deformable surface framework that will be used in the remaining of this paper. Among all the geometrical representations that have been proposed to model deformable surfaces (see [14, 16] for a review of this topic) we rely on a discrete surface model represented by a 3D triangular mesh. Such models have the advantage of being computationally efficient in comparison to finite element approaches [14]. A deformable surface is driven by the minimization of the weighting sum of an external energy which attracts the surface toward structures of interest, and an internal energy which ensures the regularity of the surface.

3.2.1 External Forces

There is a large amount of literature on methods for computing external forces and defining external energy [2]. In the original formulation, the

external energy is computed by integrating on the contour a potential derived from the image gradient [10]. Other approaches detect boundary points along vertex normals by using a gradient-based criterion [15]. In some cases, a region-based criterion is used to improve the reliability of detections [19]. In this paper, the external energy is defined by summing, for all vertices of the mesh, the quadratic distance between the vertex and a boundary point (feature point) detected along the vertex normal

$$E_{ext} = \sum_i \|V_i - \tilde{V}_i\|^2, \qquad (2)$$

where $V_i \in \mathbf{R}^3$ is the vertex i of the deformable surface and $\tilde{V}_i \in \mathbf{R}^3$ is the detected feature point. The detection is performed up to a limited distance l from the current vertex position. A large number of force types can be designed using this formulation. For example, gradient based forces can be used by detecting high gradient values which correspond to edges. When dealing with poorly contrasted images, gradient-based information alone is often not appropriate to find relevant feature points. In such cases, it is possible to use region information to improve the robustness of feature points detection. This region information can be extracted by taking into account a sequence of consecutive profile values. In this section, we focus on a general framework description; details on feature points detection will be given in Sec. 3.5.

3.2.2 Internal Forces

Internal forces are used to maintain a homogeneous distribution of vertices over the mesh and to ensure the regularity of the surface. Two types of forces are described in the following paragraphs.

• **Smoothing constraint**

These forces are typically used when no statistical information about the shape can be built. In this paper, these forces will only be used to build a Statistical Shape Model (SSM) (see Sec. 3.5).

$$F_i^{int} = -\Delta(\Delta(V_i)), \qquad (3)$$

where F_i^{int} is the internal force at vertex i and $\Delta(.)$ is the discretized laplacian operator on the mesh

$$\Delta(V_i) = \frac{1}{C_i} \sum_{j \in c(i)} V_j - V_i. \qquad (4)$$

$c(i)$ is the set of indexes of all vertices in a k-neighborhood of the vertex i and C_i is the number of elements of $c(i)$. We use $k = 3$.

• **Shape constraint**

These forces are used when an anatomical reference is available [29]. They ensure that the shape of the deformable model stays close to the shape of the anatomical reference (so called *attractor*).

$$F_i^{int} = \Delta(V_i) - \Delta(V_i^{att}), \qquad (5)$$

where V_i^{att} is the vertex position i of the attractor mesh V^{att}. It is important to note that the attractor mesh V^{att} and the deformable mesh V are topologically identical i.e. the two meshes must have the same number of triangles, and those triangles must be connected in the same way.

3.2.3 Deformation Process

A common drawback of deformable models is the energy minimization which becomes a tedious task when the mesh has a large number of vertices. Indeed, the more the number of vertices

increases, the more often the energy has local minima. To overcome this limitation we proposed a method, inspired from a popular technique, the Free Form Deformation (FFD) technique [22]. FFD relies on the use of a regular control lattice to define a 3D space warping. Then, by moving control points, surfaces can be readily animated. The main advantage in using FFD techniques is that these methods implicitly impose smoothness on the deformation. Moreover, this technique is computationally efficient even for meshes with a large number of vertices. However, although FFD has very attractive properties, there is no direct regularization of the shape. This weakness forbids the incorporation of prior knowledge about the shape and thus makes the use of such a model not adapted to medical image segmentation. In this paper, the deformable model is driven by internal forces computed as described in Sec. 3.2.2 and external forces computed by incrementally deforming a control lattice that overlaps the surface. The evolution process is realized in four steps iterated until convergence:

Deformation process
Iterate until convergence

1. **Control grid initialization:** *We adopt the B-Spline geometric transformation to model the FFD. The compact support of B-Spline yields to computationally efficient algorithms. The control lattice is initialized to overlap the current deformable surface and such that the underlying displacement function $T(p, x) : \Omega_G \to \mathbf{R}^3$ is null for all $x \in \Omega_G$, where p is the vector of control points. Consequently all elements of p are null. Note that the boundaries of Ω_G are iteratively recomputed to overlap the de-*

formable surface.

2. **Feature points detection:** *The detection of boundary points $\tilde{V}_i$ is performed on each profile i of the deformable model using some suitable detectors (see Sec. 3.3). Boundary or region based information can be used as explained previously.*

3. **Incremental FFD estimation:** *the external energy (Eq. 2) is minimized by finding nodes displacements on the control lattice. To do so, we use a single iteration of gradient descent. Let Δp be the vector of control points after the gradient descent. The external force $F_i^{ext}(t)$ is then defined as the vector proportional to the FFD displacement obtained at the vertex position $V_i(t)$*

$$F_i^{ext}(t) = T(\Delta p, V_i(t)).$$

4. **Deformable model reconfiguration:** *First, internal forces are computed for each vertex of the mesh. Then, the model is updated by combining external forces to internal forces :*

$$V_i(t + 1) = V_i(t) + \Delta t(F_i^{ext}(t) + \alpha F_i^{int}(t)),$$

where Δt is the time step that is tuned to 1.0 and α is a parameter that weights the strength of the internal forces.

3.3 Feature Detection

In this section, we give more details about the detection of boundary points. The quality of the segmentation obtained using deformable models highly depends on the ability to extract the correct feature points from the data. However, the choice of a feature detector remains a difficult
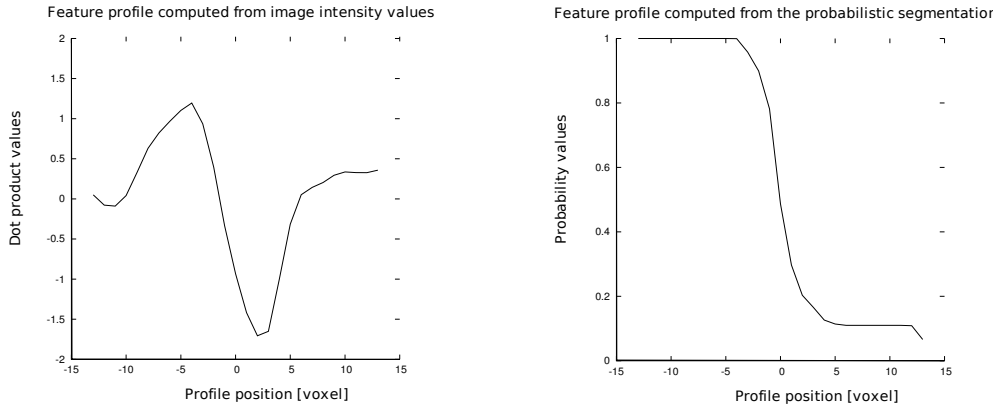
9

Figure 4: **Example of feature values computed along a vertex normal at a particular location of the mesh. (a)** feature values computed from the image data using the dot product between the image gradient orientations and the vertex normal (f^k in Sec. 3.3.1); **(b)** feature values computed from the *probabilistic segmentation* by interpolation of probability values (g^k in Sec. 3.3.2)

task when the image is poorly contrasted, with ill-defined boundaries or "false boundaries". In these cases, the detection of simple features, such as ridges or edges often produces outliers [21].

To overcome these drawbacks, we propose to use the *probabilistic segmentation* coming from the atlas registration. This probabilistic segmentation is used to define a *spatial constraint* that improves the robustness of *feature point* detection by ensuring that detected points stay in likely positions.

The detections are based on the minimization of an objective function defined for each vertex of the mesh. The feature point $\tilde{V}_i = V_i^{\hat{k}}$ is searched along the vertex normal such that

$$\hat{k} = \arg\min_{k=-l,...,l} E_i(k), \quad V_i^k = V_i + kh\vec{n_i}, \quad (6)$$

where l is the capture range, h is inter-point distance on the profile and $\vec{n_i}$ is the surface normal at vertex i. The objective function is composed

of a term that measures the quality of the model fit to the image data (Image Feature Model) and a term that measures the quality of the model fit to the probabilistic segmentation (Spatial Constraint Model)

$$E_i(k) = E_i^{im}(k) + \gamma E_i^c(k), \quad (7)$$

where, the parameter γ weights the strength of the spatial constraint. The influence of the parameter γ on the segmentation accuracy is presented in Fig. 6 and discussed in Sec. 4.2.

3.3.1   Image Feature Model

In this paper, the local image appearance around the vertex V_i of the deformable surface is described by a profile of feature values extracted from the image. The profile values are extracted at different positions from the vertex V_i along the normal direction $\vec{n_i}$. More formally, the profile centered at a position V along a direction $\vec{n}$

10

is defined by a feature vector $f(V, \vec{n})$ of length $M = 2m + 1$

$$f^k(V, \vec{n}) = \frac{\nabla I(V + d^k).\vec{n}}{\sum_k |\nabla I(V + d^k).\vec{n}|}, \quad k = 0, ..., M-1, \tag{8}$$

where

$$d^k = h(k - m)\vec{n}. \tag{9}$$

f^k is the kth element of the feature vector and $\nabla I(x)$ is the gradient image. The dot product of the vertex normal and the image gradient orientations is an interesting feature for detecting interest points approximately situated in the normal direction. The normalization that appears in Eq. 8 is used in order to be more robust to illumination changes. Fig. 4 illustrates a profile of feature values f^k.

To build an image appearance model, we require a training set of K annotated images where corresponding points have been marked on each example. More precisely, we assume having a set of K meshes with corresponding vertices representing the segmentation of the prostate in different images. The determination of these correspondences is addressed in Sec. 3.5. Then, for each vertex, we compute from the training set, the mean feature profile $\bar{f}_i$ and the covariance matrix Σ_i^f.

$$\bar{f}_i = \frac{1}{K}\sum_j f_{ij}, \quad \Sigma_i^f = \frac{1}{K}\sum_j (f_{ij} - \bar{f}_i)(f_{ij} - \bar{f}_i)^T, \tag{10}$$

where $f_{ij} = f(V_{ij}, \vec{n}_{ij})$ is the feature vector extracted at the vertex position V_{ij} (the vertex position i of the shape j) along the surface normal $\vec{n}_{ij}$ (the surface normal i of the shape j). The image energy for the vertex i is then computed using the Mahalanobis distance

$$E_i^{im}(k) = \mathbf{e}^T \Sigma_i^{f-1} \mathbf{e}, \quad \mathbf{e} = f(V_i^k, \vec{n_i}) - \bar{f}_i$$

where $V_i^k = V_i + kh\vec{n}_i$. In practice, the Mahalanobis distance is approximated using only the most significant eigenmodes of the covariance matrix [4].

3.3.2 Spatial Constraint Model

The probability map $P(x)$ (Eq. 1) represents the probability of finding the prostate at a specified position, for a subject that has been aligned to the atlas image $\bar{I}(x)$. Mapping this probability map to the patient anatomy using the inverse registration transform provides a *probabilistic segmentation* of the subject. i.e. the probability of finding the prostate at a specified location in the subject's anatomy. The local smoothness or sharpness of this *probabilistic segmentation* brings precious information on the location of the prostate boundary. We propose to use this information to improve the robustness of feature points detection and prevent the surface from leaking into unlikely configurations.

This *spatial constraint* is obtained by introducing another type of profile $g(V, \vec{n})$ whose values are obtained by bilinear interpolation of the *probabilistic segmentation*. To build the *spatial constraint model*, we require a training set of K annotated *probabilistic segmentations* where corresponding points have been marked on each example. To do so, we consider the training set introduced in the previous section that is composed of K images associated with K meshes corresponding to the segmentation of the prostate in each image. A set of *probabilistic segmentations* is obtained by registering each training image to the anatomical atlas. Then, for each vertex i, we compute the mean feature profile $\bar{g}_i$ and the covariance matrix Σ_i^g. Fig. 4 illustrates a profile of feature values g^k. Finally, the *spatial constraint* energy is computed using the Maha-

11

lanobis distance

$$E_i^c(k) = \mathbf{e}^T \Sigma_i^{g-1} \mathbf{e}, \quad \mathbf{e} = g(V_i^k, \vec{n_i}) - \bar{g}_i \quad (11)$$

3.4   Coarse to Fine Reconfiguration

A strong motivation for using deformable models is the incorporation of prior knowledge on the shape of segmented structures. In this paper, we rely on a Point Distribution Model (PDM) for statistical shape analysis. A PDM is a parametric representation of a set of learning shapes, where each shape is represented by a set of corresponding points [3]. Sec. 3.5 gives a description of the method used to compute correspondences across the learning shapes. Each shape is encoded into a shape vector, and the covariance matrix of training vectors is computed. Then, a compact parametric model is generated by Principal Component Analysis (PCA). Finally, we get a parametric model that can be fitted onto the data by adding a pose transformation $\mathbf{T}$

$$X = \mathbf{T}(\bar{X} + \sum_i w_i B_i), \quad (12)$$

where $X = (X_0^T, ..., X_m^T)^T$ is the parametric shape vector with $X_i = (X_{ix}, X_{iy}, X_{iz})^T$, $\bar{X}$ is the mean shape and B_i are the eigenmodes. $\mathbf{T}(X) = (A(X_0)^T, \ldots, A(X_N)^T)^T$ is the pose transformation that performs an affine transformation A of each point X_i. To prevent the algorithm from falling into non-optimal solutions, we use a *coarse to fine* approach that progressively increases the degrees of freedom of the deformable model.

In a first step, we rely on a parametric approach (ASM) that consists in finding the weights of eigenmodes (w_i) and the pose transformation $\mathbf{T}$ that fits the PDM to the detected boundary points [4]. The boundary points detection is carried out as described in Sec. 3.3.

After a fixed number of reconfigurations (25 iterations), we rely on the deformable model framework presented in Sec. 3.2 using the shape constraint presented in Sec. (3.2.2). This shape constraint ensures that the deformable mesh stays close to an *anatomical reference.* In this paper, we chose this reference by iteratively projecting the current shape of the deformable model onto the shape space spanned by the PDM. More formally, the energy in Eq. 5 is extended as follows:

$$F^{int}(t) = \Delta(V_i(t)) - \Delta(\hat{X}_i(t)), \quad (13)$$
$$\hat{X}^t = \arg\min_{T, w_i} \sum_i \|X_i - V_i(t)\|$$

where $V_i(t)$ is the vertex position i of the deformable surface at iteration t and $\hat{X}(t)$ is the *anatomical reference* for the shape constraint at iteration t. This strategy increases the number of degrees of freedom of the deformable model, comparatively to an ASM approach, while ensuring a statistical constraint that prevents the surface from leaking in unlikely configurations. In Eq. 13 the *anatomical reference* $\hat{X}(t)$ corresponds to the best approximation of the deformable mesh $V(t)$ by the PDM. The boundary point detections that drive the evolution process (see Sec .3.2) are realized as for the previous parametric approach but reducing the capture range l in order to further improve the robustness of the deformable model. In this way, boundary detections become more local as the degrees of freedom of the deformable model increase.

A summary of parameter setting for the deformable model is presented in table 1.

12

Table 1: **Parameter setting of the Deformable Surface Model.**

Parameter	Value
Energy weight, α	1.0
Spatial constraint weights, γ	0.5
Capture range for ASM evolution, l	8
Capture range for *Shape Constraint* evolution, l	4

3.5 Computing Correspondences Across Shapes

In this section, we briefly describe a method for establishing correspondences across shapes represented by 3D triangular meshes. These correspondences are necessary to build the PDM (Sec. 3.4), the Image Feature Model (Sec. 3.3.1) and the Spatial Constraint Model (Sec. 3.3.2).

For each patient of the learning-set, a patient specific mesh is built by deforming a generic prostate mesh to a set of points manually placed on the prostate boundaries. The procedure yields to a set of meshes with corresponding vertices. The generic prostate mesh used in this paper is the triangulation of the average prostate shape that is used for initialization purposes in Sec. 3.1. To model the mesh deformation, we rely on the deformable model framework presented in Sec. 3.2 with the smoothing constraint (Eq. 5).

The resulting meshes are then used to construct a PDM, as described in Sec. 3.4. Next, for each vertex, two distinct feature models are constructed by exploiting information coming from patient images and from *probabilistic segmentations*. The probabilistic segmentations are obtained by registering each patient image to the *probabilistic atlas* prior to model construction.

The statistical analysis leads to the *Image Feature Model* (see Sec. 3.3.1) and the *Spatial Constraint Model* (see Sec. 3.3.2). It is important to note that the *template mesh* used for establishing correspondences across shapes is the same as the one used for the initialization of the deformable model in the Sec. 3.1. In this way, initialization of level 2 is straightforward, since the template mesh propagated by the registration transform of the level 1 can be directly used as the starting point of the mesh evolution.

4 Results and Conclusion

Validation has been carried out on a data-set composed of 36 MR exams (T2-weighted – Spin Echo) acquired with a 1.5 Tesla (T) scanner using a surface coil. All exams were acquired on patients before prostate biopsy with TRUS control guidance. The acquisition was realized with a voxel size of about $0.5mm \times 0.5mm \times 3.3mm$. Note that small variations around this voxel size can be observed in the data-set. Before atlas construction, all exams are resampled with a voxel size of $1.0mm \times 1.0mm \times 1.0mm$. Numerical results presented are based on a leave-one-out cross-validation : the tested image was removed from the data-set used to construct the model.

13

Table 2: **Performance Measure - Cross Validation on 36 patients**. Level 1 represents segmentation results after atlas matching. Level 2 represents segmentation results after surface evolution. PPV: Positive Predictive Value. Sens: Sensitivity. DSC: Dice Coefficient. Mean: Mean surface error in (mm). Max: Max surface error in mm. RMSD: Root Mean Square Deviation of the surface error in (mm).

| Level | ALL GLAND | | | | | |
	PPV	Sens	DSC	Mean	RMSD	Max
1	0.78	0.87	0.80	3.14	2.41	11.15
2	0.84	0.86	0.84	2.41	1.97	9.04

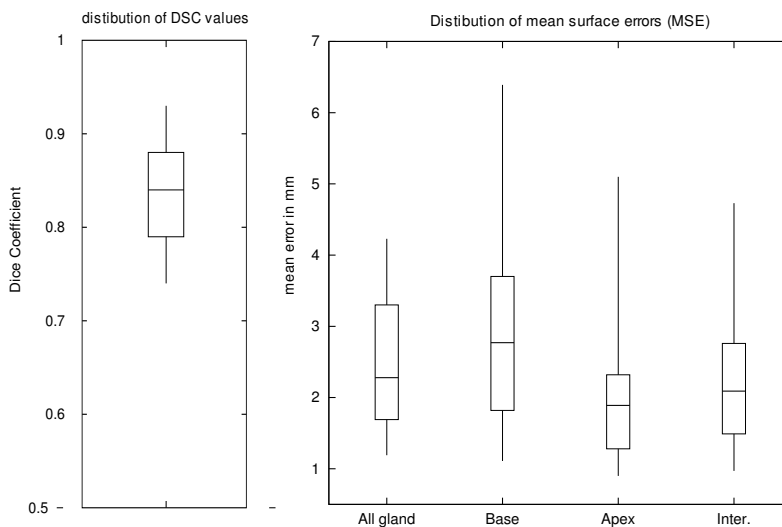| Level | BASE | | | APEX | | | INTER. | | |
	Mean	RMSD	Max	Mean	RMSD	Max	Mean	RMSD	Max
1	4.06	2.41	10.84	2.24	1.40	5.77	2.85	2.26	10.09
2	3.12	2.07	8.46	1.87	1.16	4.79	2.11	1.71	7.83

Figure 5: **Distribution of accuracy measures over the tested population.** This was assessed using Dice Coefficient (DSC) and mean surface errors (MSE) between manual and expert segmentations. MSE values are computed for the entire gland, for the base of prostate, for the apex of the prostate and for the region in between. The boxplots illustrate the distribution of DSC values or MSE values : The bound of each box represents the 25th and 75th percentile of the random distribution. The median value is represented by a line dividing the box. The smallest and largest values are connected to the box with a vertical line.
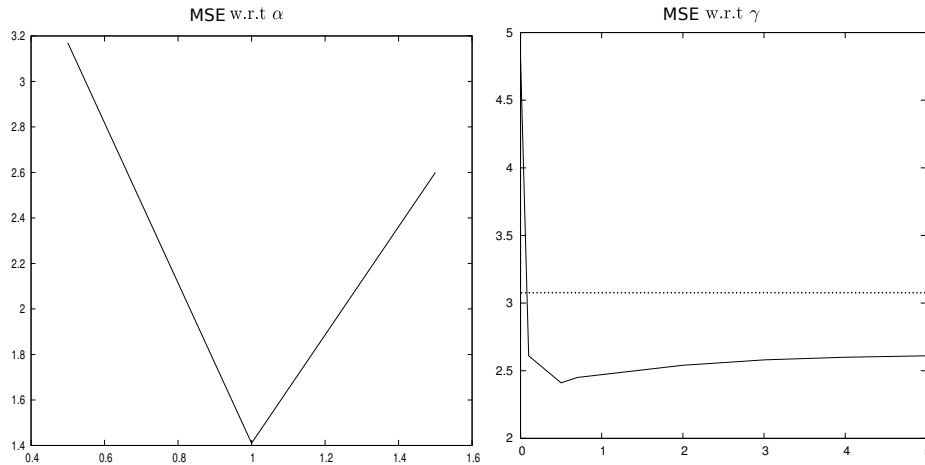
Figure 6: **Influence of parameters α and γ on the segmentation accuracy**. The parameter α tunes the strength of the *shape constraint*, and the parameter γ tunes the relative influence of the *Image Feature Model* and the *Spatial Constraint Model*. The graph (A) plots the average MSE (level 1 + level 2) against α for $\gamma = 0.5$. The graph (B) plots the average MSE against γ for $\alpha = 1.0$. The dashed lines represent the average MSE value obtained after atlas matching (level 1 only).
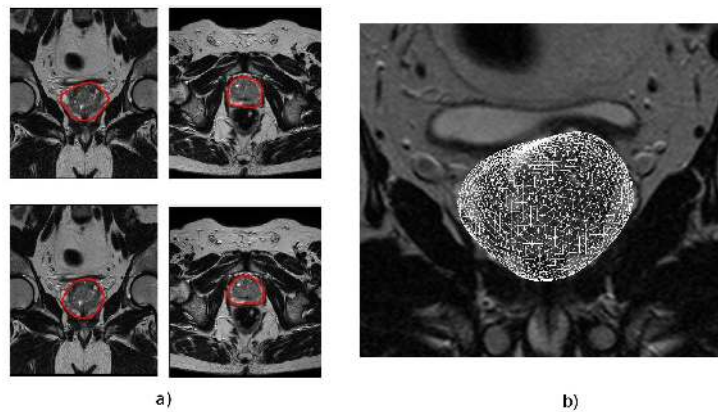

Figure 7: **Example of resulting segmentation**. (a) top row, manual segmentation; bottom row, corresponding automatic segmentation (b) 3D view of the prostate mesh

15

Numerical results are based on the comparison of the automatic segmentation to the segmentation of a single expert. We have used voxel-based overlap measures : Positive Predictive Value (PPV), Sensitivity (Sens), Dice Coefficient(DSC)

$$PPV = \frac{TP}{TP + FP}, \quad Sens = \frac{TP}{TP + FN}, \quad (14)$$
$$DSC = \frac{2TP}{TP + FP + TP + FN}$$

where TP, FN and FP are, respectively, the number of true positives, false negatives, and false positives. We also measured the similarity between triangular meshes (automatic segmentation and manual segmentation) using the maximum, the mean and the Root Mean Square Deviation (RMSD) of surface errors. Surface errors were computed by finding the shortest Euclidean distance between each vertex of the manual segmentation and the surface of the automatic segmentation. Average values of similarity measures are reported in Tab. 2.

4.1 Results for level 1

Over the 36 exams, a mean surface error of 3.14 mm and a mean RMSD of 2.41 mm was achieved. The mean dice coefficient (DSC) value was 0.80 and the mean sensitivity and Positive Predictive Values were 0.87 and 0.78, respectively.

It appeared that exams which were "far from the anatomical atlas" were more difficult to segment. To illustrate this issue, we proposed to evaluate the distance between a given subject and the anatomical atlas by measuring the amount of displacement needed to register the two images. We then computed the correlation score between the amount of displacement and the segmentation accuracy. We found a value of 0.61 with a segmentation accuracy measured using the mean surface error (MSE) and the amount deformation $\mathcal{D}$ computed using the following formula : $\mathcal{D} = \sum_{x \in \Omega_A} d(x)^2$. Where $d(x)$ is the displacement obtained at the voxel x of the atlas domain Ω_A. Note that measuring the distance between two images is a complex issue often encountered in multi-atlas methods, and that other criteria could be potentially used (for instance intensity-based measures).

The prostate was roughly divided into three regions : the apex, the base and the intermediate region in between. Surface-based measures of accuracy were realized separately on these regions. One can observe large differences between regions. Over the 36 exams, the MSE values at the apex and in the intermediate region were significantly smaller than at the base (t-test;p=0.0015). The average MSE values for these 3 regions were of 2.24 mm, 2.85 mm and 3.93 mm, respectively. In contrary, the MSE values at the base and in the intermediate region did not show statistical difference (t-test; p=0.23). The relatively large errors occurring at the base can be explained by the lack of strong edges in the interface between the prostate and the seminal vesicles. In the vicinity of the interface, the two regions share the same type of textures. Moreover, the atlas is not accurate in this region because bladder-filling heavily varies across the tested data-set (see Fig. 2). As a result, atlas matching can be difficult in this region.

4.2 Results for level 2

An example of an automated segmentation result is presented in Fig. 7. Results show a significant improvement of MSE values (t-test; p=0.0015), RMSD values (t-test; p=0.06) and max errors

(t-test; p=0.03) comparatively to level 1. The average values for these 3 measures are respectively of 2.41 mm ($\Delta = -0.73mm$), 1.97 mm ($\Delta = -0.44mm$) and 9.04 mm($\Delta = -2.11mm$). Level 2 also significantly improves the DSC values (t-test; p=0.05) comparatively to level 1, with an average DSC value of 0.84 ($\Delta = -0.04$). One can also observe a significant improvement of MSE values at the base (t-test,0.03), the apex (t-test; p=0.06) and the intermediate region (t-test, p=0.002).

After the second stage, prostate segmentation is fairly accurate across the population, with a median DSC of 0.87. These results are close to the manual segmentation accuracy. In [11] a median inter-observer DSC of 0.87 was evaluated using 3 different experts. It should be noticed that our results are biased by the use of a single expert for the accuracy measurements. An evaluation based on the comparison of the automatic segmentation with a "gold standard" generated by combining several expert segmentations should probably change notably in our favor the accuracy measurements.

The influence of deformable model parameters (α et γ) on the mean DSC is reported in Fig. 6.

The measured computation time is around 4 min (for level 1 and 2) on a PC Dual Core 1.6 GHz (2 GB RAM) running with Linux. The application has been coded in C++. Although the automated segmentations are fairly accurate, in clinical practice, they may need corrections, if they are required for planning. However, these corrections could be done easily by using a deformable model driven by user-supplied points. As the segmentation method is completely automatic, all computations can be done without the need of a clinician.

4.3   Discussion

In [11] an automatic prostate segmentation including the seminal vesicles is presented. The method was evaluated on 50 MRI exams with a voxel size of 0.5 mm × 0.5 mm × 1 mm (in this work the voxel size is about 0.5 mm × 0.5 mm × 3.3 mm). Results are evaluated by comparing the automatic segmentation with a "gold standard" generated by combining 3 expert segmentations. In the best setting, a median DSC of 0.85 is reported. This is very close to our method that achieves a median DSC of 0.87. In our previous work [12], we proposed a semi-automatic method for the segmentation of 17 MR scans acquired with an endorectal probe. Over the 17 MR scans, the average value of means surface errors (MSE) was 3.39mm. The current method achieves an average MSE of 2.41mm on 36 MR scans. In this paper, the segmentation accuracy is improved compared to our previous work, by the use of a deformable surface that uses more prior information to achieve the segmentation (an image appearance model, a statistical shape model and a spatial constraint model). [1] presents a prostate segmentation method without vesicles, which is validated on 24 3D MR exams. A mean volume overlap ($VO = (X \bigcap Y)/(X \bigcup Y)$) of 0.78 is reported, where X is the automatic segmentation and Y is the the expert segmentation. This measure corresponds to a mean DSC of 0.88 ($DSC = 2VO/(VO + 1)$), that is somewhat better than our results (mean Dice of 0.84) but the method is semi-automatic. In [30] a hybrid 2D/3D ASM is used to segment 26 3D MRI scan. A mean RMSD of 5.5 mm with a standard deviation of 2.9 mm is reported. This value has been computed using to slice by slice analysis. Our method achieves a mean RMSD computed

in 3D of 1.97 mm with a standard deviation of 0.94 mm. However, the RMSD value reported in [30] would be lowered if computed in 3D.

Contrary to the methods previously proposed in the literature that use, either deformable surfaces or anatomical atlases, our algorithm couples the two types of methods. Atlas-based methods are robust, but not suitable to introduce a priori information on the shape of the structures to be segmented. However, atlas-based methods are useful for providing information on the localization of the structures of interest (probabilistic segmentation). By using the probabilistic segmentation during the second level, we fully exploit the information provided by the probabilistic atlas. Although the presented work is limited to the use of a single anatomical atlas, the generalization in the multi-atlas case should be envisioned without changing the proposed methodology. In contrary, multi-atlas methods often search for a globally optimal segmentation, by combining a set of segmentations obtained using different atlases [11], which is roughly what our method proposes. Indeed, the probability map of the atlas is nothing more than a combination of different segmentations. Thus, the fusion step could be naturally replaced by the use of our deformable surface. This should likely be a more powerful method of combining different segmentations, since it makes use of image information and knowledge about the prostate's shape.

However, the method has some limitations and many improvements could be envisioned. First of all, as we already discussed in the paper, a multi-atlas strategy should allow to better take into account large anatomical variations. Moreover, the spatial constraint presented in this paper, that prevents the deformable surface from leaking into an unlikely configuration could possibly be improved. Indeed, the constraint force that is active during all the model evolution could be replaced by a force that is active only when a vertex is outside of an interest area. Moreover, the design of the constraint force could be envisioned using other means than the statistical analysis of surface profiles extracted from the probabilistic segmentation (may be using non-statistical modeling). Finally the design of external forces could be possibly improved by using other image features or other statistical modeling.

4.4 Conclusion

This paper has presented a fully automatic prostate segmentation of MR images technique. The segmentation is achieved in two stages. In the first stage, the new patient to be segmented is registered to a probabilistic atlas using an affine followed by a demons based registration. A *probabilistic segmentation* of the prostate is obtained by mapping the probability map of the atlas to the patient anatomy thanks to the registration transform.

In the second stage, a deformable surface refines the previously obtained segmentation. The deformable model is driven by the detection of boundary points along surface profiles. To improve the reliability of these detections, we rely on the use of an *Image Feature Model* coupled with *Spatial Constraint Model*. The *Spatial Constraint Model* prevents detections from occurring in unlikely spatial positions thanks to the *probabilistic segmentation*. A coarse-to-fine approach that progressively increases the degree of freedom of the deformable model is used to prevent the algorithm from converging to a non-optimal solution.

The validation has been carried out using a

cross validation on 36 patients. Results are fairly accurate and close to the expert segmentation accuracy with a median DSC of 0.87. The deformable model greatly refines the segmentation obtained using the atlas, by reducing the mean errors from 3.14 mm to 2.41 mm ($\Delta = -0.41$mm; p=0.0015).

Most serious errors occur for prostates which are dissimilar to the atlas (as pointed out by the correlation score between the segmentation accuracy and the amount of displacement of the non-rigid transformation). This is mainly due to the fact that a single atlas cannot take into account large anatomical variations between subjects. We are very confident in improving the segmentation accuracy in these cases using several atlases instead a single one. A multi-atlas strategy should result in an improvement in the segmentation accuracy in the first segmentation stage, which should have great effect on the accuracy of the final segmentation.

References

[1] N. Betrouni, A.S. Dewalle, P. Puech, M. Vermandel, and J. Rousseau. 3d delineation of prostate, rectum and bladder on mr images. *Computerized Medical Imaging and Graphics*, 32(7):622–630, 2008.

[2] L.D. Cohen and I. Cohen. Finite-element methods for active contour models and balloons for 2-D and 3-D images. *IEEE Transactions on Pattern Analysis and Machine Intelligence*, 15(11):1131–1147, 1993.

[3] T.F. Cootes, C.J. Taylor, D.H. Cooper, J. Graham, et al. Active shape models-their training and application. *Computer vision and image understanding*, 61(1):38–59, 1995.

[4] TF Cootes, CJ Taylor, A. Lanitis, DH Cooper, and J. Graham. Building and using flexible models incorporating grey-level information. In *Computer Vision, 1993. Proceedings., Fourth International Conference on*, pages 242–246, 1993.

[5] M.J. Costa, H. Delingette, S. Novellas, and N. Ayache. Automatic segmentation of bladder and prostate using coupled 3d deformable models. *Lecture Notes in Computer Science*, 4791:252, 2007.

[6] J. Crook, M. McLean, I. Yeung, T. Williams, and G. Lockwood. MRI-CT fusion to assess postbrachytherapy prostate volume and the effects of prolonged edema on dosimetry following transperineal interstitial permanent prostate brachytherapy. *Brachytherapy*, 3(2):55–60, 2004.

[7] M.R. Engelbrecht, H.J. Huisman, R.J.F. Laheij, G.J. Jager, G.J.L.H. van Leenders, C.A. Hulsbergen-Van De Kaa, J.J. de la Rosette, J.G. Blickman, and J.O. Barentsz. Discrimination of prostate cancer from normal peripheral zone and central gland tissue by using dynamic contrast-enhanced MR imaging. *Radiology*, 229(1):248, 2003.

[8] M.G. Harisinghani, J. Barentsz, P.F. Hahn, W.M. Deserno, S. Tabatabaei, C.H. van de Kaa, J. de la Rosette, and R. Weissleder. Noninvasive detection of clinically occult lymph-node metastases in prostate can-

cer. *New England Journal of Medicine*, 348(25):2491, 2003.

[9] A. Jemal, R. Siegel, E. Ward, T. Murray, J. Xu, and M.J. Thun. Cancer statistics, 2007. *CA: a cancer journal for clinicians*, 57(1):43, 2007.

[10] M. Kass, A. Witkin, and D. Terzopoulos. Snakes: Active contour models. *International journal of computer vision*, 1(4):321–331, 1988.

[11] S. Klein, U.A. van der Heide, I.M. Lips, M. van Vulpen, M. Staring, and J.P.W. Pluim. Automatic segmentation of the prostate in 3D MR images by atlas matching using localized mutual information. *Medical Physics*, 35:1407, 2008.

[12] S. Martin, V. Daanen, and J. Troccaz. Atlas-based prostate segmentation using an hybrid registration. *International Journal of Computer Assisted Radiology and Surgery*, 3(6):485–492, 2008.

[13] J. Mazziotta, A. Toga, A. Evans, P. Fox, J. Lancaster, K. Zilles, R. Woods, T. Paus, G. Simpson, B. Pike, et al. A probabilistic atlas and reference system for the human brain: International Consortium for Brain Mapping (ICBM). *Philosophical Transactions of the Royal Society of London. Series B*, 356(1412):1293, 2001.

[14] T. McInerney and D. Terzopoulos. Deformable models in medical image analysis: a survey. *Medical image analysis*, 1(2):91–108, 1996.

[15] J. Montagnat and H. Delingette. Volumetric medical images segmentation using

shape constrained deformable models. *Lecture Notes in Computer Science*, pages 13–22, 1997.

[16] J. Montagnat, H. Delingette, and N. Ayache. A review of deformable surfaces: topology, geometry and deformation. *Image and Vision Computing*, 19(14):1023–1040, 2001.

[17] L.G. Nyu and J.K. Udupa. On standardizing the MR image intensity scale. *image*, 1081, 1999.

[18] H. Park, P.H. Bland, and C.R. Meyer. Construction of an abdominal probabilistic atlas and its application in segmentation. *IEEE Trans. Med. Imaging*, 22(4):483–492, 2003.

[19] A. Pitiot, H. Delingette, P.M. Thompson, and N. Ayache. Expert knowledge-guided segmentation system for brain MRI. *NeuroImage*, 23:85–96, 2004.

[20] C. Reynier, J. Troccaz, P. Fourneret, A. Dusserre, C. Gay-Jeune, J.L. Descotes, M. Bolla, and J.Y. Giraud. MRI/TRUS data fusion for prostate brachytherapy. Preliminary results. *Medical Physics*, 31:1568, 2004.

[21] M. Rogers and J. Graham. Robust active shape model search. *Lecture Notes in Computer Science*, pages 517–530, 2002.

[22] D. Rueckert, LI Sonoda, C. Hayes, D.L.G. Hill, M.O. Leach, and D.J. Hawkes. Non-rigid registration using free-form deformations: application to breast MR images. *IEEE Transactions on Medical Imaging*, 18(8):712–721, 1999.

[23] J. Scheidler, H. Hricak, D.B. Vigneron, K.K. Yu, D.L. Sokolov, L. Huang, C.J. Zaloudek, S.J. Nelson, P.R. Carroll, and J. Kurhanewicz. Prostate cancer: localization with three-dimensional proton MR spectroscopic imaging-clinicopathologic study. *Radiology*, 213(2):473, 1999.

[24] D. Shen, Y. Zhan, and C. Davatzikos. Segmentation of prostate boundaries from ultrasound images using statistical shape model. *IEEE Transactions on Medical Imaging*, 22(4):539, 2003.

[25] R. Stefanescu, X. Pennec, and N. Ayache. Grid powered nonlinear image registration with locally adaptive regularization. *Medical Image Analysis*, 8(3):325–342, 2004.

[26] J.P. Thirion. Image matching as a diffusion process: an analogy with Maxwell's demons. *Medical Image Analysis*, 2(3):243–260, 1998.

[27] R. Toth, P. Tiwari, M. Rosen, A. Kalyanpur, S. Pungavkar, and A. Madabhushi. A multi-modal prostate segmentation scheme by combining spectral clustering and active shape models. In *Medical Imaging 2008: Image Processing. Edited by Reinhardt, Joseph M.; Pluim, Josien PW Proceedings of the SPIE*, volume 6914, pages 69144S–69144S, 2008.

[28] G.M. Villeirs, K. L. Verstraete, W.J. De Neve, and G.O. De Meerleer. Magnetic resonance imaging anatomy of the prostate and periprostatic area: a guide for radiotherapists. *Radiotherapy and Oncology*, 76(1):99–106, 2005.

[29] J. Weese, M. Kaus, C. Lorenz, S. Lobregt, R. Truyen, and V. Pekar. Shape constrained deformable models for 3D medical image segmentation. *Lecture notes in computer science*, pages 380–387, 2001.

[30] Y. Zhu, S. Williams, and R. Zwiggelaar. A hybrid ASM approach for sparse volumetric data segmentation. *Pattern Recognition and Image Analysis*, 17(2):252–258, 2007.